Dynamic End Effector Tracking With an Omnidirectional Parallel Aerial Manipulator

Karen Bodie, Marco Tognon, and Roland Siegwart

***Abstract*—To address the challenge of precise, dynamic and versatile aerial manipulation, we present an aerial manipulation platform consisting of a parallel 3-DOF manipulator mounted to an omnidirectional tilt-rotor aerial vehicle. The general modeling of a parallel manipulator on an omnidirectional floating base is presented, which motivates the optimization and detailed design of the aerial manipulator parameters and components. Inverse kinematic control of the manipulator is coupled to the omnidirectional base pose controller with a dynamic compensation term, going beyond common decoupled approaches. This presents a baseline for the control of redundant omnidirectional aerial manipulators. Experimental flights show the advantages of an active manipulator vs. a fixed arm for disturbance rejection and end effector tracking performance, as well as the practical limitations of the dynamic compensation term for fast end effector trajectories. The results motivate future studies for precise and dynamic aerial manipulation.**

***Index Terms*—Aerial systems: mechanics and control, motion control, dynamics.**

Fig. 1. Omnidirectional delta-based parallel aerial manipulator.

I. Introduction

AERIAL manipulators have a strong practical appeal in research and industry for their promise to extend dextrous interaction to an unbounded workspace [1].

The addition of a robotic arm to a flying robot increases the overall number of degrees of freedom (DOF) of the system, allowing for tasks that are otherwise impossible. For underactuated aerial platforms (able to control their position and yaw angle only), a manipulator with at least 2 DOF (e.g., a gimbal mechanism) is required to track a 6D end effector trajectory. The recent development of multi- and omnidirectional thrust aerial robots that are fully-actuated (able to control both their position and orientation) permits shifting some of the required DOF to the floating base [2]–[4]. This further enables 6D end effector trajectory tracking, and interaction with the environment via a static arm [5]–[7]. To extend manipulation capabilities and overcome actuation limits of uni-, multi- and omnidirectional thrust vehicles, different serial arm designs, in single or double arm configuration, have been proposed [8]–[10]. For such systems, different control strategies have been designed including fully-decoupled [11], [12], flatness-based [13], and full-body control [14].

Although serial manipulators have been the dominant choice thus far in aerial manipulation because of their low complexity and large workspace, parallel manipulators offer the alternative advantages of joint error averaging, reduced inertia of moving manipulator parts, and effort distribution over all motors [15]. These properties make parallel manipulators particularly suitable for local dynamic motion of the end effector within the platform's "infinite" workspace. Commonly referred to as the "macro-micro manipulator" model [16], it is sufficient to design a manipulator workspace that can compensate for the natural fluctuations of the aerial base while providing a margin for dynamic motion as required by the task. To improve end effector precision for point-contact tasks, standard unidirectional thrust aerial vehicles have been equipped with parallel manipulators for operations below [11], [17], [18] or beside [12], [19]–[21] the flying robot. In such examples, the manipulator is considered as a pure kinematic system and thus controlled with a standard inverse kinematic method to compensate for the positioning errors of the aerial platform. The dynamic coupling effects between the arm and the aerial vehicles are considered negligible, and compensated by the aerial platform relying on robust position controllers. This simplifies the control strategy, but performance degrades when rapid motions of the end effector are required, possibly leading to instability in extreme cases. Furthermore,

Manuscript received February 24, 2021; accepted July 13, 2021. Date of publication August 4, 2021; date of current version August 26, 2021. This letter was recommended for publication by Associate Editor G. Loianno and Editor P. Pounds upon evaluation of the reviewers' comments. This work was supported by the National Center of Competence in Research on Digital Fabrication, and Armasuisse Science and Technology. *(Corresponding author: Marco Tognon.)*

The authors are with the Autonomous Systems Lab, ETH Zurich, 8092 Zurich, Switzerland (e-mail: karen.bodie@mavt.ethz.ch; mtognon@ethz.ch; rsiegwart@ethz.ch).

This article has supplementary downloadable material available at https://doi.org/10.1109/LRA.2021.3101864, provided by the authors.

Digital Object Identifier 10.1109/LRA.2021.3101864

common solutions based on underactuated flying platforms consider the control of the end effector position only. Extra DOF must be added to control the end effector attitude as well.

To fill the mentioned gaps, we propose a novel aerial manipulator (see Fig. 1) consisting in an omnidirectional tilt-rotor flying base equipped with a 3 DOF parallel manipulator. We chose the morphology known as *"Clavel's Delta"* [22] because of its non-redundant 3 DOF, and rotary actuators which are easily integrated into our omnidirectional aerial robot [23]. In this letter we go beyond the state of the art, aiming at dynamic and precise end effector motion in the full 6D space. To this end, we present a novel design, modeling and control of an *omnidirectional aerial parallel manipulator*. Our contributions can be summarized as follows:

- Extension of parallel aerial manipulators to an omnidirectional flying base, showing the performance improvement over a fixed arm for 6D end effector trajectories.
- Formulation of the dynamic model of a floating base parallel manipulator, proposing relevant model simplifications validated by real experiments.
- Formulation of a control structure that compensates dynamic effects of the arm with a properly computed feed forward term, and experimental evaluation of the resulting free-flight tracking performance.

The remainder of the letter is structured as follows. Sec. II describes the system model, Sec. III presents manipulator control approaches, Sec. IV presents the design and optimization of the aerial manipulator, Sec. V shows the system performance through a series of experimental results, and Sec. VI presents concluding statements.

II. Modeling

The model of a delta manipulator mounted to an omnidirectional floating base is derived using frames depicted in Fig. 2: $\mathcal{F}_W$ is an arbitrarily placed inertial frame such that the z-axis is opposite to the gravity vector; $\mathcal{F}_B$ is rigidly attached to the flying base at its center of gravity; $\mathcal{F}_D$ is rigidly attached to the flying base such that it is centered at the delta manipulator base and rotated π [rad] about the x-axis of $\mathcal{F}_B$. The transformation of $\mathcal{F}_D$ in $\mathcal{F}_B$ is given by a constant translation, ${}^B\boldsymbol{p}_D \in \mathbb{R}^3$, and orientation, ${}^B\boldsymbol{R}_D \in SO(3)$.

A. Kinematic Model

1) Omnidirectional Floating Base: Seeking generality, we model the floating base as a rigid body that is subject to gravity, potential external wrenches, and a controllable wrench [23]. The latter is generated by the particular actuation setup, including propellers and servomotors to generate forces (and drag moment) in different orientations. The criteria for omnidirectionality is the platform's capability of generating a wrench which can sustain hover in any orientation [24], also subject to the center of mass offset produced by an end effector in its most extended state.

The configuration of the aerial platform is given by the position and orientation of $\mathcal{F}_B$ with respect to $\mathcal{F}_W$, denoted by the vector ${}^W\boldsymbol{p}_B \in \mathbb{R}^3$ and rotation matrix ${}^W\boldsymbol{R}_B \in SO(3)$.

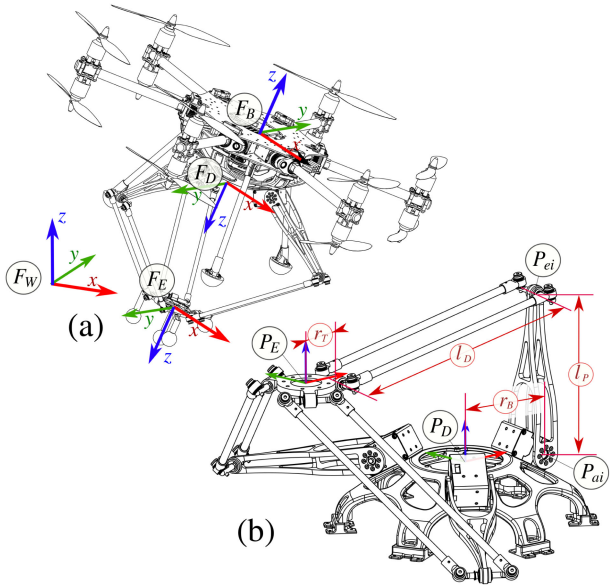

Fig. 2. (a) System model including world ($\mathcal{F}_W$), base ($\mathcal{F}_B$), delta base ($\mathcal{F}_D$), and end effector ($\mathcal{F}_E$) frames. $\mathcal{F}_D$ and $\mathcal{F}_E$ are related by a pure translation. (b) Parameter descriptions of the 3 DOF delta manipulator.

We complete the state of the aerial platform with the linear and angular velocities of $\mathcal{F}_B$ with respect to $\mathcal{F}_W$ denoted by the vectors ${}^W\boldsymbol{v}_B \in \mathbb{R}^3$ and ${}^B\boldsymbol{\omega}_B \in \mathbb{R}^3$, respectively, where the angular velocity is expressed in $\mathcal{F}_B$. We combine the pose and velocities of the flying vehicle in the variables $\boldsymbol{q}_B = ({}^W\boldsymbol{p}_B, {}^W\boldsymbol{R}_B) \in SE(3)$ and $\dot{\boldsymbol{q}}_B = [{}^W\boldsymbol{v}_B^\top \ {}^B\boldsymbol{\omega}_B^\top]^\top \in \mathbb{R}^6$.

2) Delta Manipulator: A visual description of the delta manipulator is provided in Fig. 2(b). To describe the arm configuration, the actuated joint positions $\boldsymbol{q}_D \in \mathbb{R}^3$ are chosen as generalized coordinates. In the feasible and singularity-free workspace there is a one to one correspondence between $\boldsymbol{q}_D$ and the end effector position with respect to $\mathcal{F}_D$, denoted by ${}^D\boldsymbol{p}_E \in \mathbb{R}^3$. The kinematic and differential-kinematic functions relating the actuator states (configuration and corresponding velocity) to end effector states (position and linear velocity) are well known for a 3 DOF delta parallel manipulator [22].

The forward kinematic relation, $h_E^D : \mathbb{R}^3 \to \mathbb{R}^3$, maps actuated joint positions, $\boldsymbol{q}_D$, to the end effector position, ${}^D\boldsymbol{p}_E$, such that ${}^D\boldsymbol{p}_E = h_E^D(\boldsymbol{q}_D)$. Geometric constraints require the end point of each parallel chain to be at the end effector point. These constraints are expressed by the loop closure equations $\boldsymbol{\Gamma}_i$ for each parallel chain i, with $i = \{1, 2, 3\}$. For all $i = \{1, 2, 3\}$, it should be that:

$$\boldsymbol{\Gamma}_i := ||{}^D\boldsymbol{p}_E - {}^D\boldsymbol{p}_{ai} - {}^D\boldsymbol{p}_{ei-ai}(\boldsymbol{q}_D)||^2 - l_D^2 = 0, \quad (1)$$

where P_{ai} and P_{ei} represent the point of the joint axis center and elbow frames of the i^{th} parallel chain, respectively. ${}^D\boldsymbol{p}_{ai} \in \mathbb{R}^3$ describes the position of P_{ai}, while ${}^D\boldsymbol{p}_{ei-ai} \in \mathbb{R}^3$ describes the vector between P_{ai} and P_{ei}, both expressed in $\mathcal{F}_D$. Among the solutions[1] of (1), when solving for ${}^D\boldsymbol{p}_E$, we take the one with a greater distance from $\mathcal{F}_D$, since the alternatives would

[1]The closed form solution of (1) can be found in [22].

mean passing through an uncontrollable kinematic singularity or violating physical constraints.

For the differential kinematic relations, the end effector velocity Jacobian is constructed from two matrices obtained by partially differentiating the stacked loop closure equations, $\boldsymbol{\Gamma} = [\boldsymbol{\Gamma}_1 \ \boldsymbol{\Gamma}_2 \ \boldsymbol{\Gamma}_3]^\top$:

$$\underbrace{\frac{\partial \boldsymbol{\Gamma}}{\partial {}^D\boldsymbol{p}_E}}_{\boldsymbol{A}} \delta {}^D\boldsymbol{p}_E + \underbrace{\frac{\partial \boldsymbol{\Gamma}}{\partial \boldsymbol{q}_D}}_{\boldsymbol{B}} \delta \boldsymbol{q}_D = 0. \tag{2}$$

The resulting Jacobian, $\boldsymbol{J}_D^D(\boldsymbol{q}_D) = -\boldsymbol{A}^{-1}\boldsymbol{B} \in \mathbb{R}^{3\times 3}$, maps actuated joint velocities into end effector velocity, i.e., ${}^D\boldsymbol{v}_E = \boldsymbol{J}_D^D \dot{\boldsymbol{q}}_D$. With three actuators to control 3 DOFs, the manipulator is non-redundant. Two types of kinematic singularities are present [25]: rank loss of $\boldsymbol{A}$ represents an uncontrollable end effector motion; rank loss of $\boldsymbol{B}$ represents a serial link singularity within at least one kinematic chain, where actuator motion does not lead to end effector displacement. Avoidance of singularities is discussed in Sec. IV.

Combining the pose and velocity of the flying base, together with equations (1) and (2), we derive the kinematic relations between the position and velocity of the end-effector expressed in $\mathcal{F}_W$, $({}^W\boldsymbol{p}_E, {}^W\boldsymbol{v}_E)$, and the configuration of the aerial manipulator and relative velocity, denoted by $\boldsymbol{q} = (\boldsymbol{q}_B, \boldsymbol{q}_D) \in SE(3) \times \mathbb{R}^3$ and $\dot{\boldsymbol{q}} = [\dot{\boldsymbol{q}}_B^\top \ \dot{\boldsymbol{q}}_D^\top]^\top \in \mathbb{R}^9$, respectively:

$${}^W\boldsymbol{p}_E = h_E(\boldsymbol{q}) = {}^W\boldsymbol{p}_B + {}^W\boldsymbol{R}_B \left({}^B\boldsymbol{p}_D + {}^B\boldsymbol{R}_D {}^D\boldsymbol{p}_E\right) \tag{3}$$

$${}^W\boldsymbol{v}_E = \boldsymbol{J}_{PB} {}^W\boldsymbol{v}_B + \boldsymbol{J}_{RB} {}^B\boldsymbol{\omega}_B + \boldsymbol{J}_D \dot{\boldsymbol{q}}_D = \boldsymbol{J}_E(\boldsymbol{q})\dot{\boldsymbol{q}}, \tag{4}$$

where ${}^D\boldsymbol{p}_E(\boldsymbol{q}_D) = h_E^D(\boldsymbol{q}_D)$ is computed solving (1), while $\boldsymbol{J}_{PB}$, $\boldsymbol{J}_{RB}$ and $\boldsymbol{J}_D$ are the Jacobians with respect to the components of $\dot{\boldsymbol{q}}$, where $\boldsymbol{J}_D = {}^W\boldsymbol{R}_B {}^B\boldsymbol{R}_D \boldsymbol{J}_D^D$. The Jacobians can be computed differentiating (3) and using (2) to express the linear relations with the components of $\dot{\boldsymbol{q}}$.

B. Dynamic Model

Previous works using delta-based aerial manipulators, assume low manipulator inertia and quasi-static motions, to then treat the dynamics of the manipulator as a small disturbance to the system compensated by the base controller. With the goal of dynamic motions, the inertial effects of the manipulator become non negligible and must be actively compensated by the floating base (fixed base manipulators do not suffer from the same problem thanks to passive reaction forces). Therefore, we must consider the complete dynamics of the system.

Assuming the floating base to be a pure wrench generating inertial body, and the remaining system to comprise multiple rigid bodies connected by pure rotary joints, the simplified system dynamics are those of a floating base delta manipulator. The nonlinear dynamic model of the combined system can then be derived in closed form, based on recursive algorithms for parallel manipulators. We consider the equivalent tree structure of the manipulator's parallel chains with a floating end effector as in [25], and use the projected Newton-Euler method to express generalized forces due to dynamics in the platform's base frame. This quantity which we refer to as $\boldsymbol{\delta}(\ddot{\boldsymbol{q}}, \dot{\boldsymbol{q}}, \boldsymbol{q}) \in \mathbb{R}^6$ represents the coupling wrench between the manipulator and flying base, and will be used as a compensation term in the controller. Note that to extend the delta manipulator dynamics to a floating base and to use in the projected Newton-Euler method, the acceleration kinematics must be adapted from those presented in [25] to consider the rotating base frame.

We formulate the system dynamics in Lagrangian form, with positive definite inertial matrix $\boldsymbol{M} \in \mathbb{R}^{9\times 9}$ and gravitation, centrifugal and Coriolis vector $\boldsymbol{c} \in \mathbb{R}^9$ as

$$\boldsymbol{M}(\boldsymbol{q})\ddot{\boldsymbol{q}} + \boldsymbol{c}(\boldsymbol{q}, \dot{\boldsymbol{q}}) = \boldsymbol{u}, \tag{5}$$

where $\boldsymbol{u} = [\boldsymbol{f}_B^\top \ \boldsymbol{\tau}_B^\top \ \boldsymbol{\tau}_D^\top]^\top \in \mathbb{R}^9$ are the generalized forces exerted on the body due to commanded aerodynamic forces, torques, and manipulator actuation.

The complete model considers dynamics of the passive manipulator joints, and adds significant complexity to the derivation. With the presented system construction, we make the following assumptions for model simplification:

- Elbow and wrist components have a small inertia about their rotational axis and a small change in center of mass position due to rotation. They can therefore be grouped respectively with the corresponding proximal link and the end effector platform.
- The lightweight distal links can be neglected due to their negligible mass ($10[\mathrm{g}]$ in our case) and inertial effects.

The resulting simplified model forgoes the need to compute passive joint motion, and greatly reduces the number of computations for the projected Newton-Euler method.

III. Control

To show the benefits of the delta manipulator for dynamic end effector trajectory tracking with high precision (despite positioning errors and disturbances applied to the flying base, as commonly done in the related state of the art), we consider the case in which the desired trajectories for the end effector position, ${}^W\boldsymbol{p}_E^d(t)$, and the flying base position and attitude, ${}^W\boldsymbol{p}_B^d(t)$ and ${}^W\boldsymbol{R}_B^d(t)$ are given (e.g., by an online/reactive planner). Under these conditions:

- the arm action should minimize the end effector position error given the current pose of the base;
- the flying base action should minimize its own position and attitude[2] errors.

Given the two control objectives, and employing the dynamic model of the system (see Section II), we implement a standard inverse dynamic plus linear control action. This also allows for proper compensation of the dynamic coupling effects between the flying base and robot arm. Due to weight limitations, robotic arms for aerial manipulators are normally realized with servomotors providing position or at best velocity control modes. The flying base, however, can directly control the applied wrench. The following presents how we handle the control discrepancy between the manipulator and the flying base, exploiting the derived dynamic model to compensate dynamic coupling effects.

[2]We recall that, because of the particular delta structure, the attitude of the end effector and of the flying base are the same.

A. Delta Manipulator Control

If the servomotors of the arm are controlled in position, they internally run a proportional-integral-derivative (PID) controller to track a desired position reference $\boldsymbol{q}_D^\star$, considered as input. Given the current base pose, ${}^W\boldsymbol{p}_B$ and ${}^W\boldsymbol{R}_B$, and desired end effector position ${}^W\boldsymbol{p}_E^d$, we can compute the joint references by inverting the kinematic relation[3] (3):

$$\boldsymbol{q}_D^\star = h_E^{-1}({}^W\boldsymbol{p}_B, {}^W\boldsymbol{R}_B, {}^W\boldsymbol{p}_E^d). \tag{6}$$

If the servomotors of the arm are controlled in velocity, they internally run a PI controller tracking a desired velocity reference $\dot{\boldsymbol{q}}_D^\star$, considered as input. Given the current base pose, $({}^W\boldsymbol{p}_B, {}^W\boldsymbol{R}_B)$, velocities, $({}^W\boldsymbol{v}_B, {}^B\boldsymbol{\omega}_B)$, and desired end effector position and velocity $({}^W\boldsymbol{p}_E^d, {}^W\boldsymbol{v}_E^d)$, we can compute the joint velocity references by an outer loop P controller plus a feed-forward term (inverting the differential kinematic relation):

$$\dot{\boldsymbol{q}}_D^\star = \boldsymbol{J}_D(\boldsymbol{q})^{-1}{}^W\boldsymbol{v}_{EB}^d + \boldsymbol{K}_P^D(\boldsymbol{q}_D^\star - \boldsymbol{q}_D), \tag{7}$$

where $\boldsymbol{K}_P^D \in \mathbb{R}^{3\times3}$ is a positive definite matrix,

$${}^W\boldsymbol{v}_{EB}^d = {}^W\boldsymbol{v}_E^d - \boldsymbol{J}_{PB}(\boldsymbol{q}){}^W\boldsymbol{v}_B - \boldsymbol{J}_{RB}(\boldsymbol{q}){}^B\boldsymbol{\omega}_B, \tag{8}$$

is the desired end effector linear velocity with respect to the current $\mathcal{F}_D$, and $\boldsymbol{q}_D^\star$ is computed as in (6).

It is well known that, in ideal conditions, controller (7) for velocity controlled servos is the preferred option due to the presence of the feedforward term. Unfortunately, in real implementations, servomotors have limited read/write frequency which limits the frequency of the outer controller (7), and consequently the maximum value of $\boldsymbol{K}_P^D$, resulting in reduced tracking performance. When the frequency of the outer loop controller is much slower than the internal servo controller, it is practically better to implement (6) and rely on the high rate internal position controller of the servo.

B. Omnidirectional Floating Base Control

To track the desired flying base pose we rely on an inverse dynamics approach and compensate the motion of the delta manipulator with a feedforward term. Considering the full system dynamics (5), we can rewrite the dynamics of the flying platform (the first six rows) as

$$\boldsymbol{M}_B\ddot{\boldsymbol{q}}_B + \boldsymbol{c}_B(\dot{\boldsymbol{q}}_B, \boldsymbol{q}_B) = \boldsymbol{u}_B + \boldsymbol{\delta}(\ddot{\boldsymbol{q}}, \dot{\boldsymbol{q}}, \boldsymbol{q}), \tag{9}$$

where $\boldsymbol{M}_B \in \mathbb{R}^{6\times6}$, $\boldsymbol{c}_B \in \mathbb{R}^6$, and $\boldsymbol{u}_B = [\boldsymbol{f}_B^\top \ \boldsymbol{\tau}_B^\top]^\top \in \mathbb{R}^6$ are the inertia, Coriolis and gravitational terms, and input of the flying base only. The term $\boldsymbol{\delta}$ collects all the dynamic coupling effects between the flying base and the arm. To control the flying base pose, we firstly feedback linearize (9) computing $\boldsymbol{u}_B$ as:

$$\boldsymbol{u}_B = \boldsymbol{M}_B\ddot{\boldsymbol{q}}_B^\star + \boldsymbol{c}_B(\dot{\boldsymbol{q}}_B, \boldsymbol{q}_B) - \boldsymbol{\delta}(\ddot{\boldsymbol{q}}, \dot{\boldsymbol{q}}, \boldsymbol{q}), \tag{10}$$

where $\ddot{\boldsymbol{q}}_B^\star \in \mathbb{R}^6$ is a virtual control input implementing a PID action to track the desired pose of the base, $\boldsymbol{q}_B^d(t) = ({}^W\boldsymbol{p}_B^d(t), {}^W\boldsymbol{R}_B^d(t))$. In particular,

$$\ddot{\boldsymbol{q}}_B^\star = \ddot{\boldsymbol{q}}_B^d + \boldsymbol{K}_D^B\dot{\boldsymbol{e}}_B + \boldsymbol{K}_P^B\boldsymbol{e}_B + \boldsymbol{K}_I^B\int \boldsymbol{e}_B dt, \tag{11}$$

where $\boldsymbol{K}_P^B, \boldsymbol{K}_I^B, \boldsymbol{K}_D^B \in \mathbb{R}^{6\times6}$ are standard PID positive definite gains. The pose errors are defined[4] as

$$\boldsymbol{e}_B = \begin{bmatrix} {}^W\boldsymbol{p}_B^d - {}^W\boldsymbol{p}_B \\ \frac{1}{2}\left[{}^W\boldsymbol{R}_B^{d\,\top}{}^W\boldsymbol{R}_B - {}^W\boldsymbol{R}_B^\top{}^W\boldsymbol{R}_B^d\right]^\vee \end{bmatrix} \tag{12}$$

$$\dot{\boldsymbol{e}}_B = \begin{bmatrix} {}^W\boldsymbol{v}_B^d - {}^W\boldsymbol{v}_B \\ {}^W\boldsymbol{R}_B^\top{}^W\boldsymbol{R}_B^d\,{}^B\boldsymbol{\omega}_B^d - {}^B\boldsymbol{\omega}_B \end{bmatrix}. \tag{13}$$

Notice that to implement (10), the calculation of $\boldsymbol{\delta}$ requires the accelerations of the system configuration variables. The linear acceleration of the platform can be estimated from the accelerometer, while its angular acceleration and the joint accelerations of the manipulator are computed by numerical differentiation. Due to the noisy nature of the acceleration estimation, some opportune filtering is needed. In Section V we shall show how the delay introduced by this filtering, together with those introduced by non-ideal actuation, limits the performance of the compensation solution.

IV. Aerial Manipulator Design

A. Omnidirectional Base

A tilt-rotor hexacopter is used as an omnidirectional base for the aerial manipulator. Six tiltable co-axial rotor groups are spaced evenly about the body z-axis, in the form of a conventional hexacopter. The addition of tiltable rotor groups creates a large actuation space in which thrust and torque vectors can be arbitrarily chosen, subject to motor saturation. Further details of this system design are described in [7].

B. Delta Parallel Manipulator

1) Parameter Selection: The drawback of a parallel manipulator is its limited workspace, which we can justify by careful design of the workspace volume. Since the omnidirectional floating base can achieve any pose, the workspace size must be large enough to compensate for base position error in addition to task trajectory ranges which have higher dynamics than the one the base can achieve. For this we choose a target workspace as a cube with side length $0.2[\mathrm{m}]$.

We use a genetic optimization algorithm and cost function to select the static manipulator parameters as described in [26]. The goal is to fit a cubic volume inside the reachable workspace, and minimize link lengths, while also reaching a required retraction point for landing. Formulation of the optimization problem and the resulting parameters are presented in a technical report[5].

2) Mechanical Implementation: The manipulator prototype is designed for high rigidity, minimal joint friction, and precise geometric realization. Distal link parallelograms are constructed

[3]We denote with $h_E^{-1}({}^W\boldsymbol{p}_B, {}^W\boldsymbol{R}_B, {}^W\boldsymbol{p}_E^d)$ the function that computes the manipulator joint positions to obtain a desired end effector position given the current pose of the flying base. The function is derived computing ${}^D\boldsymbol{p}_E$ from (3) to then solve (2) for $\boldsymbol{q}_D$ with $i = \{1, 2, 3\}$.

[4]The notation $[\star]^\vee$ defines the un-skew operator.

[5]See the Appendix of the document available at https://www.research-collection.ethz.ch/handle/20.500.11850/499753

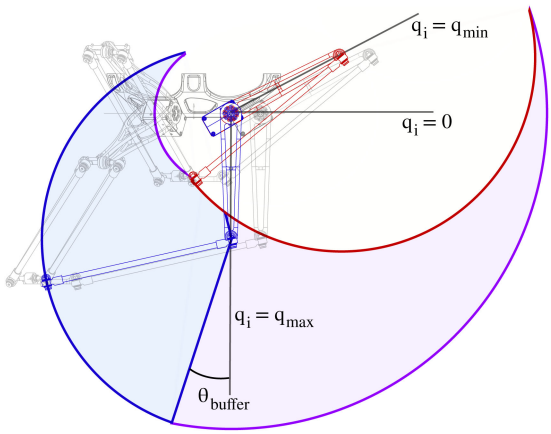

Fig. 3. Workspace visualisation of a single kinematic chain i.

using 6 rotational ball bearing joints. The proximal links, elbow, and wrist joints are precisely machined from aluminium. The distal links are hollow carbon rods, which are fixated with a length jig to reduce model error.

Final component masses are detailed in the mentioned technical report. The complete manipulator assembly including the mounting base weighs $0.72[\text{kg}]$, of which only $0.28[\text{kg}]$ is moving relative to the base. Mounted on a $4.1[\text{kg}]$ flying robot, the proportion of moving to total mass is less than 6%, confirming the inertial advantage of the parallel manipulator over a serial design. Dynamixel M430-W210 motors are selected for their sufficient torque capability and integrated position and velocity feedback.

3) Workspace Considerations: The real manipulator is subject to physical constraints, and requires avoiding singular configurations mentioned in Section II. Fig. 3 shows the limitations for an individual chain of the parallel structure, offset by the end effector plate radius such that the end of the distal link corresponds with the end effector point. For joint position q_i with a horizontal zero reference, the minimum and maximum positions q_{min} and q_{max} are due to interference with the mounting base hardware. Rotation of the distal link relative to the proximal link is limited by physical intersection with the distal link and limits of the parallelogram joints. Due to a serial chain singularity that occurs when the two links align relative to the actuated axis, the distal link is constrained to maintain a buffer angle θ_{buffer} from the singularity, preventing elbow inversion. The workspace of a single chain is the area covered by the near-hemispherical surface swept from q_{min} to q_{max}. The complete end effector workspace is the intersection of these three volumes when patterned around the $\mathcal{F}_D$ z-axis.

V. Numerical and Experimental Results

In the first set of tests we focus on showing the benefits of the delta arm for precisely tracking 6D end effector trajectories, even when the base is subjected to external disturbances. Increasing the velocities and accelerations of the desired end effector trajectory,[6] we show the limitations of purely kinematic control approaches, which motivate the use of the proposed dynamic compensation method. The second set of tests focus on highly dynamic end effector trajectories. Numerical and experimental results show the benefits of adding dynamic compensation, but also reveal some implementation and practical problems which limit its effectiveness. Visual recordings of the experimental trials are available in a supplementary video.

[6]The desired trajectory for the flying base is computed such that the one of the end effector stays in the center of the arm workspace.

Fig. 4. Experiments with the base following an arc trajectory up to 45°, and the end effector tracking a fixed point (blue circles), while a virtual disturbance force (red arrows) is applied for an active (left) and fixed (right) manipulator. .

A. Test Setup and Calibration

Tests are performed in an indoor arena equipped with a motion capture system. The Delta arm is rigidly mounted to the omnidirectional flying robot. Reflective marker constellations are installed on the flying base for state estimation, and on the manipulator for ground truth position data and for the initial calibration of the manipulator. The latter includes identifying the kinematic parameters of the delta arm, as well as the transformation between $\mathcal{F}_B$ and $\mathcal{F}_D$ using an optimization-based method reported in the mentioned technical report.

We use a multi-sensor fusion (MSF) algorithm to fuse onboard IMU data and position sensor information from a motion capture system. State estimation, control, and servo feedback operate at $200\,[\text{Hz}]$. Servo motor gains are kept at their default settings after investigating the effect of end effector tracking and reaction force measured on a force sensor test bench. The controller is implemented in C++ in a Robot Operating System (ROS) framework, and the controller setup and tuning is performed as in [7].

B. Precise 6D End Effector Tracking

1) Disturbance Rejection: A major advantage of the proposed omnidirectional manipulator is its ability to counteract disturbances in 6D, while maintaining any orientation. We show the 6D end-effector tracking capability by commanding a fixed end effector point with changing orientation, requiring the base to follow a pitching arc trajectory up to 45°. We apply a virtual disturbance force of $10[\text{N}]$ to the base along the x-axis of $\mathcal{F}_W$, then compare disturbance rejection performance for the case of a fixed manipulator, and an active delta manipulator (see Fig. 4). The tracking performance of end effector position, base position and attitude (equal to that of the end effector), shown in Fig. 5, highlight the significant reduction in end effector error when using an active delta manipulator. End effector error occurring at time $18[\text{s}]$ and $23[\text{s}]$ for the active manipulator case are due to the target point exiting the manipulator workspace.

2) End Effector Trajectory Tracking: Focusing on the effect of using an active manipulator for dynamic end effector

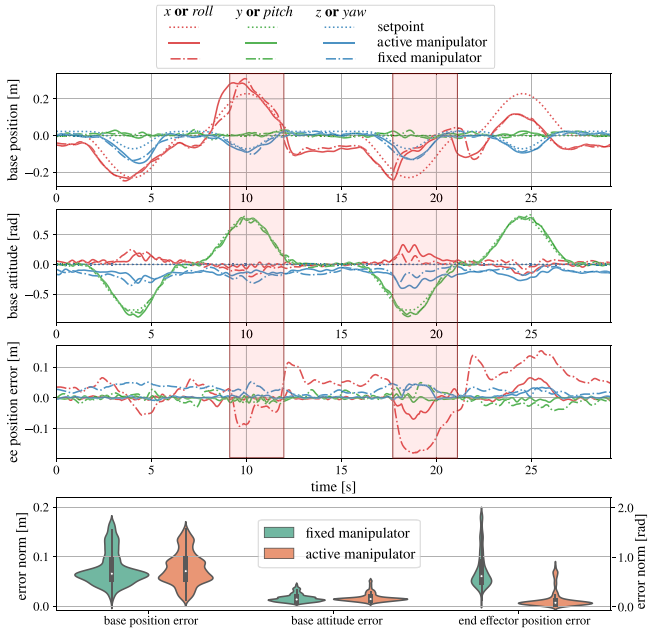

Fig. 5. Base position and orientation are plotted relative to their desired trajectory in $\mathcal{F}_W$ in the upper two plots, while the third plot shows end effector tracking error. Red blocks indicate when the disturbance force is applied. The violin plot (at the bottom) shows base and end effector tracking error distribution for the fixed and active manipulator cases.

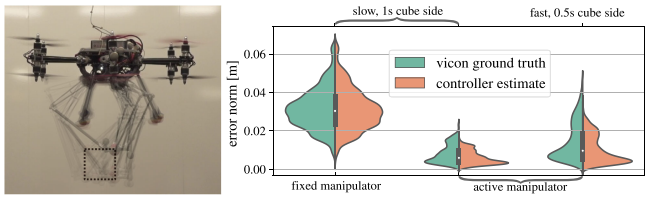

Fig. 6. Experimental setup for fast end effector tracking (left) and Violin plots (right) show the end effector tracking error for different cube trajectory speeds, for fixed and active manipulators.

tracking, we analyze the relative performance of a fixed and active manipulator for trajectories of different speeds. We command trajectories which trace the edges of a $0.1[\mathrm{m}]$ cube at $1[\mathrm{s}]$ and $0.5[\mathrm{s}]$ per edge, stopping at each vertex. Trajectories are smooth up to the acceleration level.

This series of tests is performed in the absence of dynamic compensation terms detailed in Section III-B, i.e., the control action (10) is computed with $\boldsymbol{\delta}(\ddot{\boldsymbol{q}}, \dot{\boldsymbol{q}}, \boldsymbol{q}) = 0$. This corresponds to the state of the art case where dynamic coupling effects are considered negligible. Increasing the velocities and accelerations of the desired end effector trajectory, we will show how this assumption no longer holds, degrading performance.

The norm of the tracking error plotted in Fig. 6 (error distributions) and Fig. 7 (end effector position tracking in 3D) shows the effectiveness of employing an active manipulator for position tracking. While results for slower trajectories are greatly improved with an active manipulator (norm RMSE $9.4[\mathrm{mm}]$ vs $33.2[\mathrm{mm}]$ for the fixed manipulator), the faster cube trajectory is not even achievable with a fixed arm. Because of the slower vehicle dynamics, the fast trajectory results in the system becoming

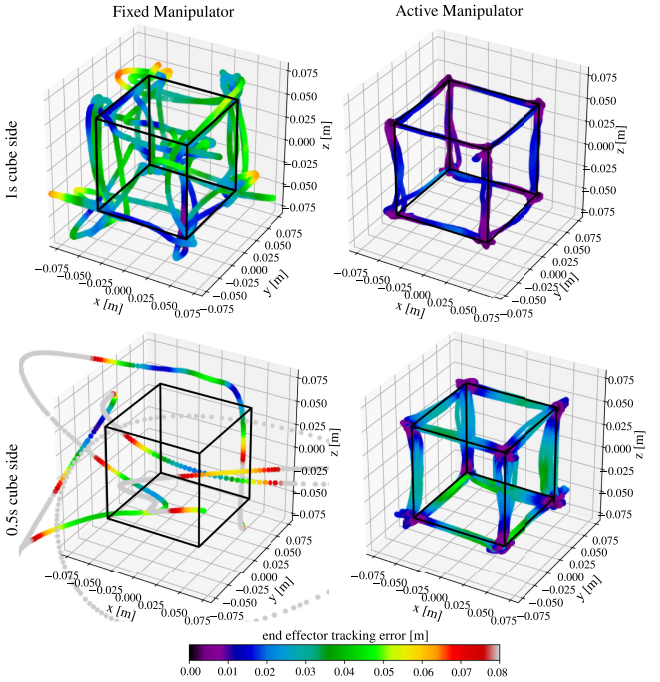

Fig. 7. End effector tracking data for 3D points, colored by the norm of position tracking error. Comparison of fixed arm tracking (left column) with active arm tracking (right column), and of slow $1[\mathrm{s}]$ (upper row) and fast $0.5[\mathrm{s}]$ (lower row) sided cube trajectory.

unstable. The active manipulator tracks the fast cube trajectory with a norm RMSE of $17.8[\mathrm{mm}]$. Looking at the right two violin plots in Fig. 6, as well as at the right tracking plots in Fig. 7, we notice degraded performance of the faster cube trajectory tracking. This effect can be explained by the non-negligible dynamics of fast end effector motion, which disturbs the motion of the base and causes a pronounced deviation from the cube edge line. This result motivates using our knowledge of the manipulator dynamics to anticipate and counteract dynamic coupling forces and torques in the base controller.

C. Fast 6D End Effector Tracking

In this section we analyze the proposed strategy to compensate dynamic coupling effects during fast end effector motion. We first experimentally validate the dynamic model derived in Section II-B, comparing the predicted dynamic coupling wrench with the readings of a force-torque sensor. We then discuss the tracking performance in both numerical and experimental tests.

1) Prediction of the Dynamic Coupling Wrench: The dynamic model is validated by mounting the delta manipulator to a 6 axis Rokubi force-torque sensor, and simultaneously exciting base and arm dynamics. We command a fast cube trajectory for the end effector in $\mathcal{F}_W$, while moving the base dynamically by hand (see Fig. 8). The complete and simplified dynamic model results are compared with ground truth data from the force-torque sensor measurements. Fig. 8 shows a segment of the predicted dynamic wrenches overlaid on the ground truth wrench readings. Results summarized in Table I show that both dynamic models closely follow the measured reaction wrench, and the

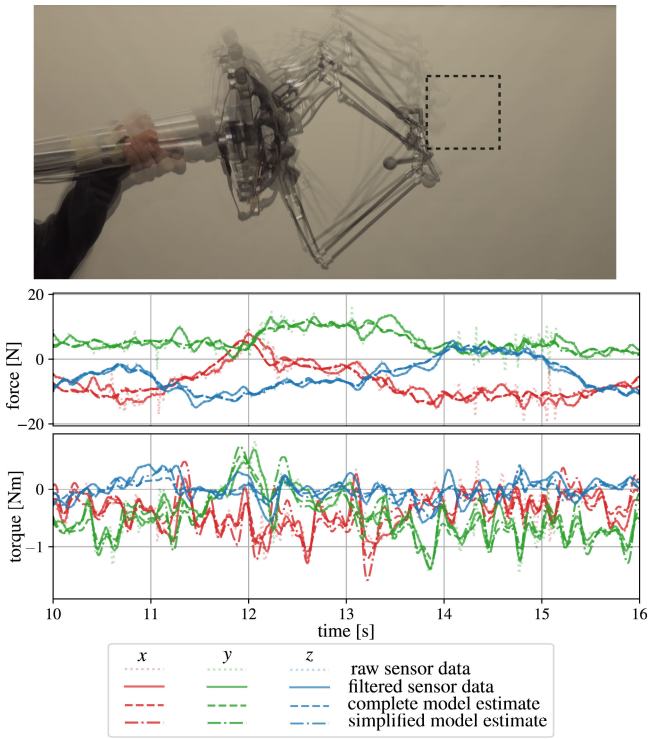

Fig. 8. Experimental dynamic model validation by dynamically moving the base while the end effector tracks a fast trajectory (top image). Plots visually compare measured forces and torques with predicted values form the simplified and complete dynamic models, expressed in $\mathcal{F}_D$ for a short segment of the test.

TABLE I
ROOT MEAN SQUARED, MEAN AND STANDARD DEVIATION OF SIMPLIFIED AND COMPLETE DYNAMIC MODEL ERROR AGAINST THE FORCE-TORQUE SENSOR MEASURED GROUND TRUTH DATA FOR 27 [s] AT 200 [Hz]. ROOT MEAN SQUARED DIFFERENCE BETWEEN MODELS IS PRESENTED IN THE THIRD ROW

		force [N]			torque [Nm]		
stat	**model**	x	y	z	x	y	z
RMS	**simp**	**2.523**	**2.217**	**1.167**	**0.207**	**0.222**	**0.117**
	comp	2.340	2.039	1.162	0.182	0.181	0.125
	diff	0.342	0.319	0.312	0.158	0.158	0.058
mean	**simp**	**0.101**	**0.075**	**-0.246**	**-0.026**	**0.006**	**0.016**
	comp	0.135	0.029	-0.174	-0.014	0.026	0.016
std	**simp**	**2.521**	**2.215**	**1.140**	**0.205**	**0.222**	**0.116**
	comp	2.336	2.039	1.149	0.182	0.179	0.124

difference between the two is very small. This result confirms that our simplifying assumptions are justified, and the error due to simplification is negligible compared to the remaining model error and noise. Remaining error is likely due to unmodeled dynamics including flexibility and vibrations, as well as noise from the force sensor measurements.

2) Simulation Results: In the following two simulation experiments we ask the aerial manipulator to track a world frame oscillating end effector 'chirp' trajectory of increasing frequency in the range of 0.5 to 2[Hz] while the base reference is fixed, with horizontal attitude. The end effector trajectory is centered at the nominal delta position in its base frame, with an amplitude of 0.1[m], first horizontally along the x-axis of $\mathcal{F}_W$ and then vertically along the z-axis. Horizontal test results are presented in Fig. 9. Vertical tests not plotted here showed similar results.

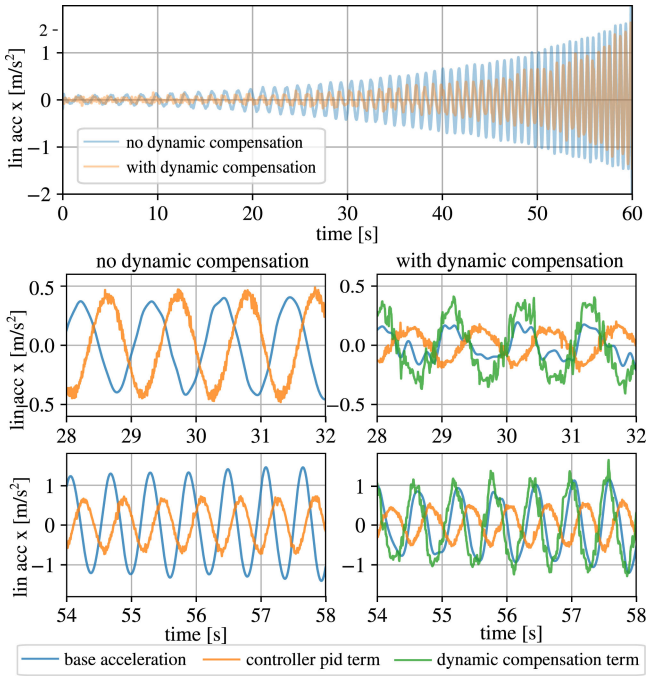

Fig. 9. Base acceleration along the excited axis is shown in the upper plot with and without feed forward dynamic compensation for a horizontally oscillating end effector trajectory of increasing frequency in simulation. In the lower two plots, a zoomed in segment of controller PID and dynamic compensation accelerations are plotted over the actual base acceleration along the excited axis.

The upper plot in Fig. 9 overlays the linear acceleration of the excited x-axis in $\mathcal{F}_W$ for the cases with and without dynamic compensation, showing the ability of dynamic compensation to reduce base acceleration towards the desired zero target, particularly for lower frequency arm trajectories. The lower four plots of Fig. 9 focus on two sections of the experiment to highlight the interplay of the base controller acceleration terms in $\mathcal{F}_B$ along the oscillating axis for cases without and with dynamic compensation. The middle plots show a region where the arm oscillates at 1[Hz], and the lower plots approaching 2[Hz]. The PID term in orange counteracts the position and velocity error caused by the moving arm, but cannot prevent the oscillation. In the middle right plot, the active dynamic compensation effectively reduces oscillations caused by 1[Hz] manipulator oscillations. At 2[Hz], however, the lower right plot indicates that the compensation term becomes less effective. We believe that this effect is the result of delays caused in part by numerical differentiation and filtering of the acceleration terms used to compute the compensation term. The effect becomes more prominent when the frequency of the coupling motion exceeds a certain threshold (approx. 2[Hz] for this system).

3) Experimental Results: We return to the fast cube trajectory from Section V-B2, and compare the performance of the active manipulator without and with the dynamic compensation term. Including dynamic compensation results in more prominent deviation from the reference edges, contrary to our intent, as shown in 3D tracking plots in Fig. 10. A number of implementation factors, such as delayed and imprecise base controller action and additional system delays, differentiate simulation results from real experiments.

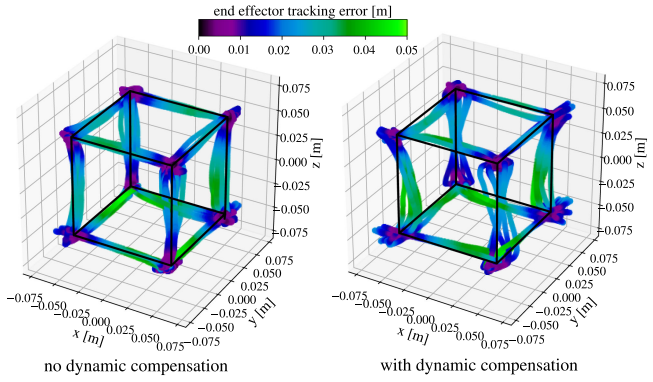

Fig. 10. 3D end effector tracking data, colored by the norm of position tracking error. Tracking of a 1[s] sided cube trajectory without (left) and with (right) dynamic compensation for an active manipulator.

This result motivates the need for future work in coupled dynamic controllers for multi-body flying systems to achieve increased end effector precision during dynamic operations.

VI. Conclusion

This letter has developed a baseline for dynamic end effector tracking with a position-redundant omnidirectional aerial manipulator. Results indicate that the parallel manipulator is an appropriate choice for dynamic floating base tracking, though limitations of dynamic compensation for fast trajectories call for further control investigation. In future work, we aim to include the complete tilt-rotor base dynamics for a whole body control approach, eventually extending to contact-based tasks.

References

[1] A. Ollero, M. Tognon, A. Suarez, D. Lee, and A. Franchi, "Past, present and future of aerial robotic manipulators," *IEEE Trans. Robot.*, to be published, doi: 10.1109/TRO.2021.3084395.

[2] M. Hamandi, F. Usai, Q. Sablé, N. Staub, M. Tognon, and A. Franchi, "Design of multirotor aerial vehicles: A taxonomy based on input allocation," *Int. J. Robot. Res.*, vol. 40, no. 8-9, pp. 1015–1044, 2021, doi: 10.1177/02783649211025998.

[3] M. Allenspach *et al.*, "Design and optimal control of a tiltrotor micro-aerial vehicle for efficient omnidirectional flight," *Int. J. Robot. Res.*, vol. 39, no. 10-11, pp. 1305–1325, 2020.

[4] M. Zhao, T. Anzai, F. Shi, X. Chen, K. Okada, and M. Inaba, "Design, modeling, and control of an aerial robot dragon: A dual-rotor-embedded multilink robot with the ability of multi-degree-of-freedom aerial transformation," *IEEE Robot. Automat. Lett.*, vol. 3, no. 2, pp. 1176–1183, Apr. 2018.

[5] S. Park *et al.*, "ODAR: Aerial manipulation platform enabling omnidirectional wrench generation," *IEEE/ASME Trans. mechatronics*, vol. 23, no. 4, pp. 1907–1918, Aug. 2018.

[6] M. Ryll *et al.*, "6D interaction control with aerial robots: The flying end-effector paradigm," *Int. J. Robot. Res.*, vol. 38, no. 9, pp. 1045–1062, 2019.

[7] K. Bodie *et al.*, "An omnidirectional aerial manipulation platform for contact-based inspection," *Robot.: Sci. Syst. XV*, vol. 15, 2019.

[8] M. Tognon *et al.*, "A truly-redundant aerial manipulator system with application to push-and-slide inspection in industrial plants," *IEEE Robot. Automat. Lett.*, vol. 4, no. 2, pp. 1846–1851, Apr. 2019.

[9] A. Suarez, G. Heredia, and A. Ollero, "Physical-virtual impedance control in ultralightweight and compliant dual-arm aerial manipulators," *IEEE Robot. Automat. Lett.*, vol. 3, no. 3, pp. 2553–2560, Jul. 2018.

[10] M. Ä. Trujillo, J. R. Martínez-de Dios, C. Martín, A. Viguria, and A. Ollero, "Novel aerial manipulator for accurate and robust industrial NDT contact inspection: A new tool for the oil and gas inspection industry," *Sensors*, vol. 19, no. 6, 2019, Art. no. 1305, [Online]. Available: https://www.mdpi.com/1424-8220/19/6/1305/htm.

[11] P. Chermprayong, K. Zhang, F. Xiao, and M. Kovac, "An integrated delta manipulator for aerial repair: A new aerial robotic system," *IEEE Robot. Automat. Mag.*, vol. 26, no. 1, pp. 54–66, Mar. 2019.

[12] D. Tzoumanikas, F. Graule, Q. Yan, D. Shah, M. Popovic, and S. Leutenegger, "Aerial manipulation using hybrid force and position NMPC applied to aerial writing," *Robot.: Sci. Syst. XVI*, 2020.

[13] M. Tognon, B. Yüksel, G. Buondonno, and A. Franchi, "Dynamic decentralized control for protocentric aerial manipulators," in *Proc. IEEE Int. Conf. Robot. Automat.*, Singapore, 2017, pp. 6375–6380.

[14] G. Nava, Q. Sablé, M. Tognon, D. Pucci, and A. Franchi, "Direct force feedback control and online multi-task optimization for aerial manipulators," *IEEE Robot. Automat. Lett.*, vol. 5, no. 2, pp. 331–338, Apr. 2020.

[15] L.-W. Tsai, *Robot Analysis: The Mechanics of Serial and Parallel Manipulators*. Hoboken, NJ, USA: Wiley, 1999.

[16] A. Sharon, N. Hogan, and D. E. Hardt, "The macro/micro manipulator: An improved architecture for robot control," *Robot. Comput.-Integr. Manuf.*, vol. 10, no. 3, pp. 209–222, 1993.

[17] G. B. Haberfeld, D. Sun, and N. Hovakimyan, "Stabilization and optimal trajectory generation for a compact aerial manipulation system with a delta-type parallel robot," in *Proc. Int. Conf. Unmanned Aircr. Syst.*, 2018, pp. 1091–1100.

[18] M. Kamel, K. Alexis, and R. Siegwart, "Design and modeling of dexterous aerial manipulator," in *Proc. IEEE/RSJ Int. Conf. Intell. Robots Syst.*, 2016, pp. 4870–4876.

[19] M. Fumagalli, S. Stramigioli, and R. Carloni, "Mechatronic design of a robotic manipulator for unmanned aerial vehicles," in *Proc. IEEE/RSJ Int. Conf. Intell. Robots Syst.*, 2016, pp. 4843–4848.

[20] T. W. Danko, K. P. Chaney, and P. Y. Oh, "A parallel manipulator for mobile manipulating UAVs," in *Proc. IEEE Int. Conf. Technol. Practical Robot Appl.*, 2015, pp. 1–6.

[21] M. Fumagalli *et al.*, "Developing an aerial manipulator prototype: Physical interaction with the environment," *IEEE Robot. Automat. Mag.*, vol. 21, no. 3, pp. 41–50, Sep. 2014.

[22] R. Clavel, "A fast robot with parallel geometry," in *Proc. Int. Symp. Ind. Robots*, 1988, pp. 91–100.

[23] K. Bodie *et al.*, "Active interaction force control for contact-based inspection with a fully actuated aerial vehicle," *IEEE Trans. Robot.*, vol. 37, no. 3, pp. 709–722, Jun. 2021.

[24] M. Tognon and A. Franchi, "Omnidirectional aerial vehicles with unidirectional thrusters: Theory, optimal design, and control," *IEEE Robot. Automat. Lett.*, vol. 3, no. 3, pp. 2277–2282, Jul. 2018.

[25] S. Briot *et al.*, "Dynamics of parallel robots," *From Rigid Bodies to Flexible Elements*. Berlin, Germany: Springer, 2015.

[26] M. Laribi, L. Romdhane, and S. Zeghloul, "Analysis and dimensional synthesis of the delta robot for a prescribed workspace," *Mechanism Mach. Theory*, vol. 42, no. 7, pp. 859–870, 2007.